Ocean Engineering 195 (2020) 106723

Contents lists available at ScienceDirect

Ocean Engineering

journal homepage: www.elsevier.com/locate/oceaneng

Numerical model for the fluid–structure interaction mechanics of a suspended flexible body

Tatsuyuki Ueda, Yoshiki Nishi *

Department of Systems Design for Ocean-Space, Faculty of Engineering, Yokohama National University, 79-5 Tokiwadai, Hodogaya, Yokohama, Japan

ARTICLE INFO

Keywords:
Fluid–structure interaction
Suspended body
Vortex-induced vibration
Wake oscillator model
Numerical model

ABSTRACT

This study investigates the dynamic vibration and static deformation of a long flexible underwater body suspended from the ocean surface. A numerical model is constructed by considering (i) the structural mechanics, (ii) hydrodynamic forces induced by vortex shedding, (iii) motion mechanics associated with the free bottom end of the suspended body, and (iv) the interactions among (i)-(iii). Numerical computations are performed by applying uniform vertical distributions of the ocean flow speed and a sheared distribution, and by varying the weight of the body at the free bottom end. Comparing the computed results of these cases elucidates the mechanics of the fluid–structure interaction of the suspended body. In particular, the sheared flow velocity profile allows the growth of multiple frequency components of vibrations in the flexible body. The frequency multiplicity at a point in the body arises from the vortex-induced vibrations excited at that point, and those that are excited in other regions then propagate to that point.

1. Introduction

Very long flexible bodies are used to convey oil and gas from the seabed to floating platforms on the ocean surface. These flexible bodies are often subjected to factors that excite motions and deformations, thereby complicating the process of resource development or production. Reliable designs are essential in ensuring operational integrity.

Sometimes, these bodies are suspended from the ocean surface (Bai and Bai, 2005), with their bottom ends hanging free under the water. For example, when a drilling riser is used in a harsh environment such as an environment prone to high waves, its bottom end is intentionally disconnected from the wellhead when the environmental conditions become too severe, while its top end remains connected to the floating platform. Therefore, it is critical to ensure safe operation in both suspended and normal conditions; the normal condition means that both ends of the flexible body are connected to other bodies in the vicinity.

Previous studies have noted the contribution of hydrodynamic forces to the excitation of vibrations of a suspended body. For example, Patel and Jesudansen (1987) experimentally examined the dynamic motion of a free-hanging riser and identified the vortex-induced force as a source of motion excitation. Meanwhile, using a perturbation technique, Triantafyllou and Triantafyllou (1991) obtained the natural modes of a free-hanging string and regarded them as the configuration of responses of the body to excitation. In their model test, Kajiwara and Noridomi (2009) observed the vibratory motion of a riser model during re-entry operations. Wenbo et al. (2014) constructed a numerical model to simulate the dynamics of a platform and drilling riser in suspended conditions.

Other previous studies have considered external forces other than the vortex-induced force acting on a suspended body. For example, Yanbin et al. (2014a,b) analytically examined the static deformation and dynamic motion of a suspended body induced by wind, waves, and vessel motion. Honghai et al. (2016) analyzed the process wherein vessel motion causes a suspended body to vibrate, and Wang et al. (2012) numerically studied the vibration of suspended bodies excited by vessel motion because of the wind and waves.

Optimal control theory applications to risers during re-entry operation have been extensively studied. For example, Shengwei et al. (2016) attempted to optimize the re-entry of a free-hanging riser, Suzuki et al. (1993, 1994) used thrusters to actively control the motion of a vessel and deepwater risers, and Ohtsubo et al. (2005) and Koterayama et al. (2008) used gain-scheduled control to improve the re-entry operation of a marine riser.

The preceding literature review shows that, compared to the motion of a floating platform in waves, vortex-induced vibration (VIV) has attracted less attention among researchers interested in the dynamics of suspended bodies. Nevertheless, because poor weather can extend the flexible body suspension time, the severity of damage and fatigue

* Corresponding author.
E-mail address: nishi-yoshiki-rg@ynu.ac.jp (Y. Nishi).

https://doi.org/10.1016/j.oceaneng.2019.106723
Received 20 April 2019; Received in revised form 4 October 2019; Accepted 10 November 2019
Available online 15 November 2019

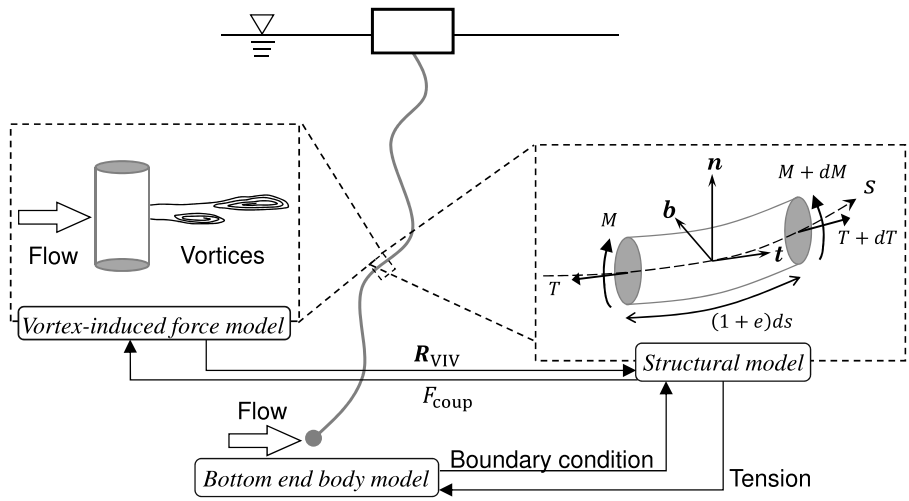

Fig. 1. Schematic of coupling between structural, vortex-induced force, and bottom end body (BEB) models. The notation M denotes moment acting on a segment. $\boldsymbol{t}$, $\boldsymbol{n}$, and $\boldsymbol{b}$ denote the tangential, normal, and binormal unit vectors of a segment, respectively.

accumulation while the body is suspended should be addressed in equal measures as that during operations in normal conditions.

This study attempts to develop a numerical simulation method to investigate the mechanics of suspended bodies undergoing VIV. Numerical simulation methods were developed to examine the mechanics of risers in normal conditions (e.g., Chatjigeorgiou (2008, 2010), Srinil (2011), Yanbin et al. (2014b), Doan and Nishi (2015), Tsukada and Morooka (2016), Honghai et al. (2016)). However, a numerical simulation method that is able to serve as a practical approach for the suspended conditions as well as the normal conditions has not been constructed. The establishment of such a numerical simulation method would allow long flexible bodies to be designed in a refined way. Considering the good performances of the finite-difference scheme (Chatjigeorgiou, 2008) and the wake oscillator model (Violette et al., 2007; Nishi et al., 2009; Doan and Nishi, 2015; Nishi and Doan, 2015) for the normal condition, this study attempts to develop a numerical computation program applicable to the suspended conditions based on the scheme and model.

To simulate the suspended conditions, the bottom end must be carefully treated. While a riser is suspended, it often has a small attachment at its bottom end, such as the lower marine riser package for a drilling riser (Bai and Bai, 2005) or the body attached to the bottom end of a vertical cold-water pipe used in ocean thermal energy conversion (Wilson, 2002). The body connected to the bottom end of the long flexible body may change the natural frequencies of the flexible body through changing the tension. Therefore, the bottom end body (BEB) should be regarded as an important design parameter.

The BEB, which behaves like an almost-rigid body, must be modeled as an independent body from the long flexible body above it. Accordingly, the model built in this study involves three sets of mechanics and the interactions between them, namely (i) structural mechanics expressing the elasticity of the suspended body, (ii) fluid mechanics expressing the vortex formation and shedding, and (iii) motion mechanics of the BEB.

Incorporating spatial differences is essential when considering the speed of fluid flow around a body that has a vertical length of a few kilometers. The VIV of the body in a sheared vertical profile of flow speeds is an unresolved issue of interest, despite attempts having been undertaken to elucidate the mechanics in sheared flows (e.g., Vandiver et al. (1996), Trim et al. (2005), Chen et al. (2015), Nishi and Doan (2015), Nishi et al. (2018)). Furthermore, these studies devoted little attention to the suspended condition. Therefore, this study investigates the following issues by interpreting the results of numerical simulations: how the vertical distributions of ocean flow speed affect the response of the suspended body, and to what extent the presence of the BEB influences the response.

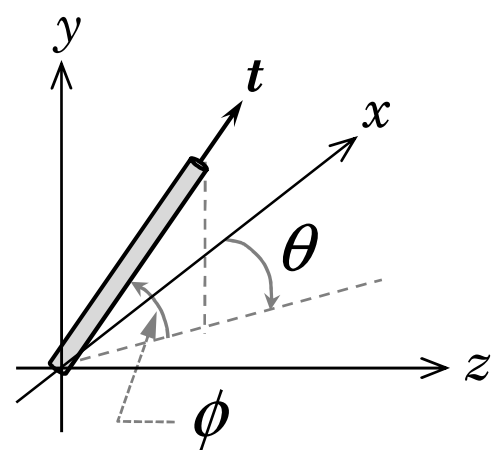

Fig. 2. Coordinate systems used to describe the governing equations. ϕ and θ denote the angles of attitude of a segment. The xyz-axes span the space-fixed coordinate system, the y-axis is vertical upward, and the xz-plane is the horizontal plane.

2. Model description

Models for the structure 2.1, the vortex-induced force 2.2 and the BEB 2.3 are described (Fig. 1). These are commonly represented using nonlinear differential equations that govern the temporal evolution of dynamic quantities. Accordingly, the numerical computational method used in this study is built to solve the equations in the time domain.

These equations are written in terms of (i) an s-coordinate system fixed to the long flexible body and extending from the bottom end ($s = 0$) to the top end ($s = L$), and (ii) an xyz-coordinate system fixed in space (Fig. 2). The variables and parameters used in the equations are listed and defined in Table 1.

2.1. Structural model

The structural model represents the deformation of the long flexible body; this body is modeled as an Euler–Bernoulli beam whose dynamics are governed by the equations of segment (a small part of the body) motion and the compatibility relation that ensures the continuity of the beam (Howell, 1992).

The equation of motion of a segment of longitudinal length $(1 + e)ds$ (see the box labeled "Structural model" in Fig. 1) has tangential,

Table 1
Notation and definitions of model variables and parameters.

Notation	Definition	Unit or value
m	Mass per unit pipe length	kg/m
m_a	Added mass per unit pipe length	kg/m
u, v, w	Velocities of a structural element in tangential, normal, and binormal directions	m/s
T	Tension	N
S_n	In-plane shear force	N
S_b	Out-of-plane shear force	N
E	Young's modulus	N/m^2
I	Area moment of inertia of pipe	m^4
A	Cross-section area of pipe	m^2
ω_0	Submerged weight per unit pipe length	kg/s^2
$e \equiv T/(EA)$	Axial strain	–
Ω_2, Ω_3	Out-of-plane and in-plane curvatures	rad
ϕ	Angle formed by tangential with the horizontal plane	rad
θ	Out-of-plane angle	rad
s	Lagrangian coordinate along the longitudinal length of body	m
ds	Longitudinal length of an unstretched segment	m
C_{dt}, C_{dn}, C_{db}	Drag coefficients in tangential, normal, and binormal directions	0.0, 1.4, 0.6
L	Whole length of suspended body	m
d	Outer diameter of suspended body	m
c_a	Added mass coefficient of circular cylinder	1.0
ρ_w	Fluid density	1.00×10^3 kg/m^3
P'	Coefficient of nonlinear damping term	–
$V \equiv \sqrt{v_c{}^2 + w_c{}^2}$	Speed of flow perpendicular to element	m/s
$\boldsymbol{V}_c \equiv (u_c, v_c, w_c)$	Flow velocity vector	m/s
f	Coefficient of the slope of the lift force	1.16
$\bar{l}$	Mean half-length of wake oscillator	$1.16d$ m
q	Width of wake oscillator	$1.25d$ m
ω_v	Natural frequency of wake oscillator	rad/s
ξ	Self-excitation coefficient	–
C_a	Added mass coefficient of BEB	0.5
C_L	Lift coefficient	–
C_{L0}	Lift coefficient of a stationary cylinder	0.4
C_D	Drag coefficient of BEB	0.4
d_B	Diameter of BEB	0.584 m
g	Gravitational acceleration	9.8 m/s^2
S	Projected area of BEB	0.184 m^2
M_a	Added mass of BEB	–
M_s	Mass of BEB in air	–
V_s	Volume of BEB	5.95×10^{-2} m^3

normal, and binormal components written as

$$m\left(\frac{\partial u}{\partial t} + w\frac{\partial \theta}{\partial t} - v\frac{\partial \phi}{\partial t}\cos\theta\right) = \frac{\partial T}{\partial s} + S_b\Omega_2 - S_n\Omega_3 - \omega_0 \sin\phi\cos\theta + (1+e)\,R_t, \tag{1}$$

$$m\left\{\frac{\partial v}{\partial t} + \frac{\partial \phi}{\partial t}(u\cos\theta + w\sin\theta)\right\} + m_a\frac{\partial v_r}{\partial t} = \frac{\partial S_n}{\partial s} + \Omega_3\left(T + S_b\tan\theta\right) - \omega_0\cos\phi + (1+e)\,R_n, \tag{2}$$

$$m\left(\frac{\partial w}{\partial t} - v\frac{\partial \phi}{\partial t}\sin\theta - u\frac{\partial \theta}{\partial t}\right) + m_a\frac{\partial w_r}{\partial t} = \frac{\partial S_b}{\partial s} - S_n\Omega_3\tan\theta - T\Omega_2 - \omega_0\sin\phi\sin\theta + (1+e)\,R_b, \tag{3}$$

where (R_t, R_n, R_b) are the components of the external force vector $\mathbf{R}$, which contains the gravity ($\mathbf{R}_w$), drag ($\mathbf{R}_d$), added mass ($\mathbf{R}_a$), and vortex-induced ($\mathbf{R}_{VIV}$) components,

$$(1+e)\,\mathbf{R} = (1+e)\left(\mathbf{R}_w + \mathbf{R}_a + \mathbf{R}_d + \mathbf{R}_{VIV}\right), \tag{4}$$

where $(1+e)\,\mathbf{R}_w$ and $(1+e)\,\mathbf{R}_a$ have tangential, normal, and binormal components described as follows:

$$(1+e)\,\mathbf{R}_w = \omega_0\left(\sin\phi\cos\theta, -\cos\phi, -\sin\phi\cos\theta\right), \tag{5}$$

$$(1+e)\,\mathbf{R}_a = -m_a\left(0, \frac{\partial v_r}{\partial t}, \frac{\partial w_r}{\partial t}\right). \tag{6}$$

The notations (u_r, v_r, w_r) are the tangential, normal, and binormal components of the relative velocity defined as $(u_r, v_r, w_r) \equiv (u - u_c, v - v_c, w - w_c)$, where (u_c, v_c, w_c) are the tangential, normal, and binormal components of the flow velocity.

The drag force $(1+e)\,\mathbf{R}_d$ has the following tangential, normal, and binormal components respectively defined as

$$R_{dt} = -\frac{1}{2}\rho_w d\pi C_{dt} u_r |u_r| \sqrt{1+e}, \tag{7}$$

$$R_{dn} = -\frac{1}{2}\rho_w d C_{dn} v_r \sqrt{v_r{}^2 + w_r{}^2}\sqrt{1+e}, \tag{8}$$

$$R_{db} = -\frac{1}{2}\rho_w d C_{db} w_r \sqrt{v_r{}^2 + w_r{}^2}\sqrt{1+e}. \tag{9}$$

The vortex-induced component $(1+e)\,\mathbf{R}_{VIV}$ is related to the lift coefficient C_L in the following manner:

$$\mathbf{R}_{VIV} = \frac{1}{2}\rho_w d V^2 C_L \frac{\boldsymbol{t} \times \boldsymbol{V}_c}{|\boldsymbol{t} \times \boldsymbol{V}_c|}, \tag{10}$$

where the temporal variation in C_L is calculated based on the vortex-induced force model as described in Section 2.2.

Segment bending is determined by the relationship between the bending stiffness, tension-induced moment, and rotational inertia. In this model, the torsional moment and the rotational inertia are omitted because they are negligible compared to the other terms. Therefore, the moment relationships can be simplified to:

$$EI\frac{\partial \Omega_2}{\partial s} = -EI\Omega_3{}^2\tan\theta + S_b\left(1 + \frac{T}{EA}\right)^3, \tag{11}$$

$$EI\frac{\partial \Omega_3}{\partial s} = EI\Omega_2\Omega_3\tan\theta - S_n\left(1 + \frac{T}{EA}\right)^3, \tag{12}$$

and the compatibility relationships can be written as

$$\frac{\partial u}{\partial s} + \Omega_2 w - \Omega_3 v = \frac{1}{EA}\frac{\partial T}{\partial t}, \tag{13}$$

$$\frac{\partial v}{\partial s} + \Omega_3\left(u + w\tan\theta\right) = \left(1 + \frac{T}{EA}\right)\frac{\partial \phi}{\partial t}\cos\theta, \tag{14}$$

$$\frac{\partial w}{\partial s} - \Omega_3 v\tan\theta - \Omega_2 u = -\left(1 + \frac{T}{EA}\right)\frac{\partial \theta}{\partial t}. \tag{15}$$

The curvatures $(\Omega_2,\ \Omega_3)$ are related to the Euler angles as

$$\Omega_2 = \frac{\partial \theta}{\partial s}, \tag{16}$$

$$\Omega_3 = \frac{\partial \phi}{\partial s}\cos\theta. \tag{17}$$

The added mass is calculated as

$$m_a = c_a\rho_w\pi\left(\frac{d}{2}\right)^2. \tag{18}$$

2.2. Model of vortex-induced force

A bluff body placed in a flowing fluid exhibits vibratory motion (e.g., Blevins (1977)), which is induced by the periodic generation and shedding of vortices in the downstream region of the body and through the interaction of vortices with the moving body. Because the section of the long flexible body addressed in this study is bluff, the fluid–structure interaction is accounted for in the present modeling.

The dynamics involved in this interaction is represented using the wake oscillator model. Although this model expresses the vortex dynamics in a simple fashion, the essence of the fluid–structure interaction mechanics is retained. Satisfactory performance of this model has been reported when simulating the VIV of riser pipes (e.g., Violette et al. (2007), Nishi et al. (2018)).

The time-varying lift coefficient, C_L, is governed by the following nonlinear equation:

$$\ddot{C}_L - 2\zeta\omega_v\left(1 - \frac{P'}{f^2}C_L{}^2\right)\dot{C}_L + \omega_v^2 C_L = F_{coup}. \tag{19}$$

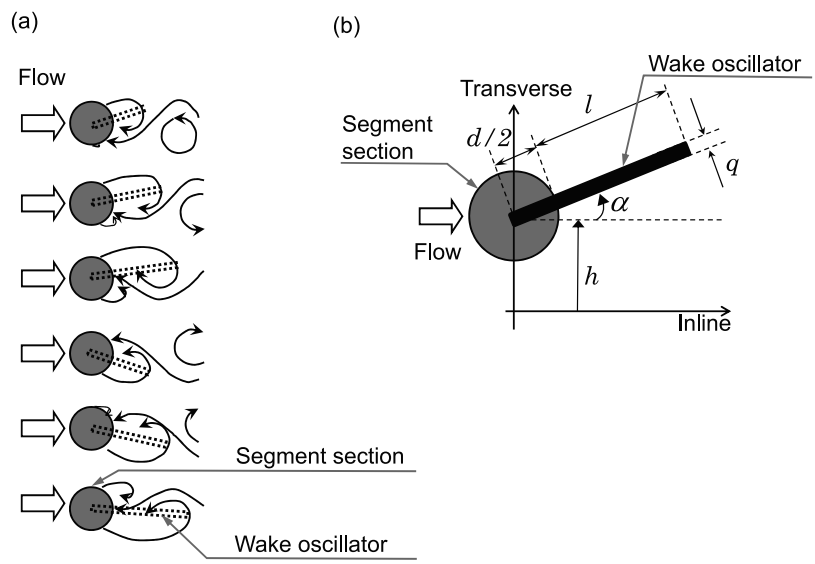

Fig. 3. Schematic of (a) vortex formation and shedding behind segment section, and (b) wake oscillator. In (b), letters "α" and "h" denote rotation and translation motions.

The term F_{coup} on the right-hand side of Eq. (19) is the force exerted by the interaction between the segment motion and the wake oscillator rotation, as expressed by

$$F_{\mathrm{coup}} \equiv \frac{f\ddot{h}}{\frac{d}{2}+\bar{l}}, \tag{20}$$

where $\ddot{\mathrm{h}}$ denotes the acceleration of the segment motion in the direction perpendicular to the flow. The present model assumes that a wake oscillator is attached to a segment (Fig. 3 and the box labeled "Vortex-induced force model" in Fig. 1).

The notation ζ is the coefficient that specifies the self-excitation intensity of the wake oscillator, defined as

$$\zeta \equiv \frac{fd}{2\sqrt{2}\pi^2\bar{l}}. \tag{21}$$

The notation ω_{v} in the third term on the left-hand side in Eq. (19) is the natural frequency of the wake oscillator. This is equivalent to the frequency of the vortex generation and shedding behind a fixed circular cylinder, defined as

$$\omega_{\mathrm{v}}^2 \equiv \frac{\pi V^2}{q\left(\frac{d}{2}+\bar{l}\right)}. \tag{22}$$

The coefficient P' represents the nonlinear damping of the wake oscillator, defined as

$$P' \equiv \left(\frac{2f}{C_{\mathrm{L0}}}\right)^2. \tag{23}$$

2.3. Model of BEB and boundary condition of structural model

The BEB is connected to the long flexible body and is assumed to be a sphere of diameter d_{B} moving in a fluid. Its motion is affected by the tension in the flexible body through the action–reaction principle. The equations of motion of the BEB in the space-fixed coordinate system (Fig. 2) are written as

$$\left(M_{\mathrm{s}}+M_{\mathrm{a}}\right)\ddot{x}_{\mathrm{B}} = T\cos\theta\cos\phi - \frac{1}{2}\rho_{\mathrm{w}}C_{\mathrm{D}}S\left|\left(\dot{x}_{\mathrm{B}}-u_{\mathrm{f}}\right)\right|\left(\dot{x}_{\mathrm{B}}-u_{\mathrm{f}}\right), \tag{24}$$

$$\left(M_{\mathrm{s}}+M_{\mathrm{a}}\right)\ddot{y}_{\mathrm{B}} = T\cos\theta\sin\phi + \left(\rho_{\mathrm{w}}V_{\mathrm{s}}-M_{\mathrm{s}}\right)g - \frac{1}{2}\rho_{\mathrm{w}}C_{\mathrm{D}}S\left|\left(\dot{y}_{\mathrm{B}}-v_{\mathrm{f}}\right)\right|\left(\dot{y}_{\mathrm{B}}-v_{\mathrm{f}}\right), \tag{25}$$

$$\left(M_{\mathrm{s}}+M_{\mathrm{a}}\right)\ddot{z}_{\mathrm{B}} = -T\sin\theta - \frac{1}{2}\rho_{\mathrm{w}}C_{\mathrm{D}}S\left|\left(\dot{z}_{\mathrm{B}}-w_{\mathrm{f}}\right)\right|\left(\dot{z}_{\mathrm{B}}-w_{\mathrm{f}}\right), \tag{26}$$

where $\left(u_{\mathrm{f}},\ v_{\mathrm{f}},\ w_{\mathrm{f}}\right)$ are the components of the flow velocity in the space-fixed coordinate system, and $\left(x_{\mathrm{B}},\ y_{\mathrm{B}},\ z_{\mathrm{B}}\right)$ are the BEB coordinates in the space-fixed coordinate system. The added mass of the BEB is calculated as

$$M_{\mathrm{a}} = C_{\mathrm{a}}\rho_{\mathrm{w}}\frac{4}{3}\pi\left(\frac{d_{\mathrm{B}}}{2}\right)^3. \tag{27}$$

The values of C_{D} (Eq. (26)) and C_{a} (Eq. (27)) are determined by referring to Sarpkaya and Isaacson (1981) and Sumer and Fredsœ (1997).

Boundary conditions must be imposed to calculate all the unknown variables in the preceding equations. The flexible body is assumed to be simply supported: the bending moments at the top ($s = L$) and bottom ($s = 0$) ends are set to zero. These conditions are written as

$$\begin{cases} \Omega_2\left(s=L,t\right)=\Omega_3\left(s=L,t\right)=0, \\ \Omega_2\left(s=0,t\right)=\Omega_3\left(s=0,t\right)=0. \end{cases} \tag{28}$$

The top end of the body is fixed, and the bottom end is positioned at the same point as the BEB, as expressed by

$$\begin{cases} u\left(s=L,t\right)=0,\ v\left(s=L,t\right)=0,\ w\left(s=L,t\right)=0, \\ u\left(s=0,t\right)=u_{\mathrm{b}},\ v\left(s=0,t\right)=v_{\mathrm{b}},\ w\left(s=0,t\right)=w_{\mathrm{b}}, \end{cases} \tag{29}$$

where $(u_{\mathrm{b}},\ v_{\mathrm{b}},\ w_{\mathrm{b}})$ are the tangential, normal, and binormal components of the BEB velocity, respectively, and are calculated via the coordinate-system transformation of the velocity in the space-fixed coordinate system in the following manner:

$$\begin{bmatrix} u_{\mathrm{b}} \\ v_{\mathrm{b}} \\ w_{\mathrm{b}} \end{bmatrix} = \boldsymbol{\Gamma}\begin{bmatrix} \dot{x}_{\mathrm{B}} \\ \dot{y}_{\mathrm{B}} \\ \dot{z}_{\mathrm{B}} \end{bmatrix}, \tag{30}$$

where $\boldsymbol{\Gamma}$ denotes the rotation matrix for the coordinate-system transformation and is defined as

$$\boldsymbol{\Gamma} \equiv \begin{bmatrix} \cos\phi\cos\theta & \sin\phi\cos\theta & -\sin\theta \\ -\sin\phi & \cos\phi & 0 \\ \cos\phi\sin\theta & \sin\phi\sin\theta & \cos\theta \end{bmatrix}. \tag{31}$$

2.4. Numerical computation method in time domain

This section explains the process of numerically solving the governing equations described earlier.

The partial differential equations (Eqs. (1)–(17)) of the structural model can be collectively written in matrix form as

$$\mathbf{M}\frac{\partial\mathbf{Y}(s,t)}{\partial t} + \mathbf{K}\frac{\partial\mathbf{Y}(s,t)}{\partial s} + \mathbf{F}\left\{\mathbf{Y}(s,t)\right\} = 0, \tag{32}$$

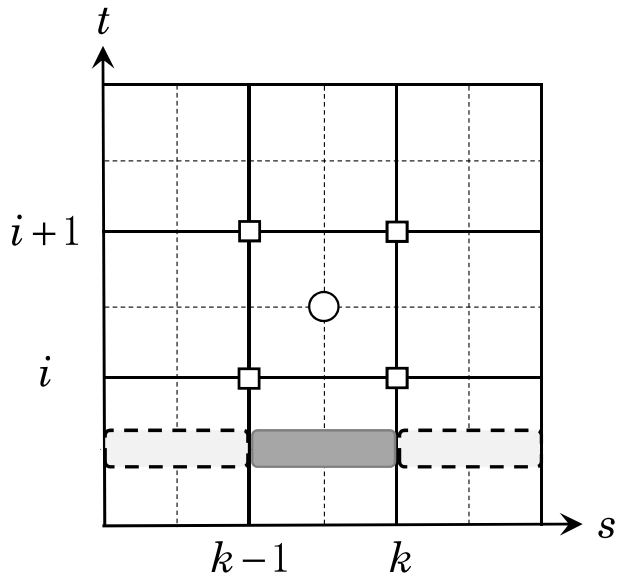

Fig. 4. Discrete points along spatial and temporal axes sequenced by integers k and i, respectively. The quantities at the locations and times represented by the open squares are used to calculate finite-difference approximations of the first-order spatial and temporal derivatives at the center (the open circle). The middle gray box represents the segment with extremities located at nodes $(k-1)$ and k, and the other two boxes are the segments connected to the middle segment.

where $\mathbf{Y}(s,t)$ is a vector containing 10 unknown variables and is defined as

$$\mathbf{Y}(s,t) \equiv \begin{bmatrix} T & S_{\mathrm{n}} & S_{\mathrm{b}} & u & v & w & \Omega_2 & \Omega_3 & \theta & \phi \end{bmatrix}^{\mathrm{T}}. \tag{33}$$

Eq. (32) is transformed into finite difference form. The second-order central finite-difference approximation is applied to both the spatial and temporal differentiations (i.e., the Kellor box method: e.g., Hoffman (1992), Fig. 4). They can be written in the following matrix form

$$\begin{aligned} &\left(\mathbf{M}_k^{i+1} + \mathbf{M}_k^{i}\right)\left(\frac{\mathbf{Y}_k^{i+1} - \mathbf{Y}_k^{i}}{\Delta t}\right) + \left(\mathbf{M}_{k-1}^{i+1} + \mathbf{M}_{k-1}^{i}\right)\left(\frac{\mathbf{Y}_{k-1}^{i+1} - \mathbf{Y}_{k-1}^{i}}{\Delta t}\right) \\ &+ \left(\mathbf{K}_{k-1}^{i+1} + \mathbf{K}_{k}^{i+1}\right)\left(\frac{\mathbf{Y}_k^{i+1} - \mathbf{Y}_{k-1}^{i+1}}{\Delta s}\right) + \left(\mathbf{K}_{k-1}^{i} + \mathbf{K}_{k}^{i}\right)\left(\frac{\mathbf{Y}_k^{i} - \mathbf{Y}_{k-1}^{i}}{\Delta s}\right) \\ &+ \left(\mathbf{F}_k^{i+1} + \mathbf{F}_{k-1}^{i+1} + \mathbf{F}_k^{i} + \mathbf{F}_{k-1}^{i}\right) = \mathbf{O}. \end{aligned} \tag{34}$$

In Eq. (34), subscripts $k-1$ and k represent the node locations on the spatial coordinate (s-coordinate) and superscripts i and $i+1$ represent the discrete times. The Kellor box method approximates a quantity and its first-order spatial and temporal derivatives at the center of the box $(i+\frac{1}{2}, k-\frac{1}{2})$ using the quantities at the four vertices surrounding the center (Fig. 4).

The ordinary differential equation in the vortex-induced force model (Eq. (19)) is solved for all the nodes placed along the long flexible body. This equation and the equations in the BEB model (Eqs. (24)–(26)) are numerically solved by applying the fourth-order Runge Kutta scheme. In the numerical computations shown herein, 201 discrete nodes are placed along the s-coordinate (the maximum of k equals 201). This means that the structure is approximated by the succession of 200 segments. Several computations were conducted by varying the number of segments to examine the effect of spatial resolution on results, confirming that the 200 segments and more yield sufficiently converged results.

2.5. Linearization and numerical computation method in frequency domain

The developed numerical method was evaluated by conducting a numerical computation in the frequency domain to ensure its appropriate performance and determine its structural design. The mathematical form of the suspended body model in the time domain was linearized, and thereafter, transformed into the form in the frequency domain. The numerical results of computations in the frequency domain were compared with the analytically determined values.

The natural frequency is very important when designing a suspended body because it is closely related to the magnitude of the VIV. Numerous studies have shown that the magnitude of the VIV corresponds to the dimensionless flow velocity (reduced velocity), which includes the natural frequency, ω_{n}, defined as

$$U^* \equiv \frac{2\pi V}{\omega_{\mathrm{n}} d}. \tag{35}$$

Each vibratory mode has its own natural frequency. The design parameters of the suspended body can be specified using the frequency-domain calculation yielding the natural frequencies.

Linearization is performed using the mathematical formula by Chatjigeorgiou (2010). The vector of unknown variables is decomposed into static $\bar{\mathbf{Y}}(s)$ and dynamic $\tilde{\mathbf{Y}}(s,t)$ components as

$$\mathbf{Y}(s,t) = \bar{\mathbf{Y}}(s) + \tilde{\mathbf{Y}}(s,t). \tag{36}$$

Assuming that the suspended body in its static state is straight and vertical, the static component comprising the zeroth-order quantities can be written as

$$\bar{\mathbf{Y}}(s) = \left[\bar{T}(s) \;\; 0\;0\;0\;0\;0\;0\;0\;0\right]^{\mathrm{T}}. \tag{37}$$

The dynamic part comprises first-order quantities of dynamic variables defined as

$$\tilde{\mathbf{Y}}(s,t) = \left[\tilde{T} \;\; \tilde{S}_{\mathrm{n}} \;\; \tilde{S}_{\mathrm{b}} \;\; \tilde{u} \;\; \tilde{v} \;\; \tilde{w} \;\; \tilde{\Omega}_2 \;\; \tilde{\Omega}_3 \;\; \tilde{\theta} \;\; \tilde{\phi}\right]^{\mathrm{T}}. \tag{38}$$

The linearized equations are derived by substituting Eq. (36) into the governing equations of the structural model (Eqs. (1)–(17)) and retaining only the first-order terms (i.e., omitting all terms equal to or higher than second-order). To transform these into equations in the frequency domain, the first-order dynamic variables are assumed to have sinusoidal temporal variations, written as

$$\tilde{\mathbf{Y}}(s,t) = \mathrm{Re}\left\{\tilde{\mathbf{y}}(s)\, e^{i\omega t}\right\}, \tag{39}$$

where ω is the frequency of the response and $\tilde{\mathbf{y}}(s)$ is the complex amplitude of the dynamic variables.

The equations that result from substituting Eq. (39) into the linearized equations are ordinary differential equations with respect to space. The equations are solved by applying the central finite-difference scheme to the spatial derivatives. The boundary conditions that the bottom and top ends are simply supported are imposed. For the calculations in the frequency domain, C_{L} in Eq. (10) is assumed to sinusoidally vary with frequency ω.

3. Results and discussion

3.1. Program evaluation

Solutions in the frequency domain were calculated by assuming the uniformity of the beam material and tension, a straight configuration, and both the ends simply supported (Fig. 5), whereupon a comparison between the theoretical and numerical results was made to verify the performance of the implemented program. The physical properties of the beam used for program evaluation are listed in Table 2. The tension is approximately 12% of the submerged weight of the beam, and is set to be small for getting neighboring two natural frequencies closer, thereby reducing the computing load in the frequency domain.

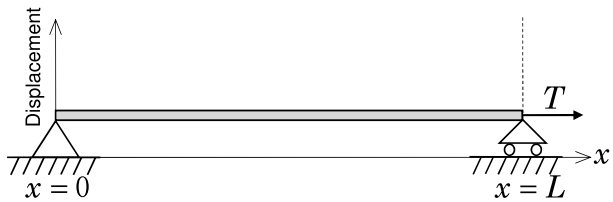

Fig. 5. Schematic of straight beam with length L, and with both ends simply supported. A constant tension, T, is loaded.

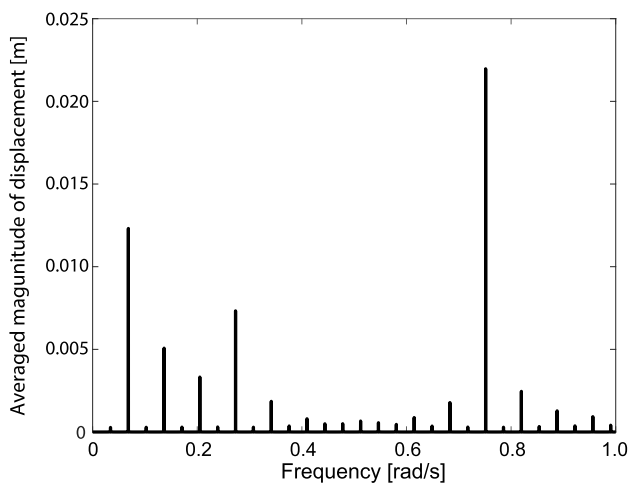

Fig. 6. Average response amplitude versus frequency of vortex-induced force.

Table 2
Physical properties of beam for program verification.

Notation	Definition	Value
L	Whole length	4000 m
d	Outer diameter	0.02 m
d_i	Inner diameter	0.01 m
E	Young's modulus	4.0×10^8 N/m^2
EI	Bending stiffness	2.945 Nm^2
EA	Axial stiffness	9.425×10^4 N
m	Mass per unit beam length	0.5184 kg/m
T	Tension	980.00 N

The theoretical solution according to these assumptions is

$$\omega_{n\_j} = \left(\frac{j\pi}{L}\right)^2 \sqrt{\frac{EI}{m}} \sqrt{1 + \frac{T}{j^2\left(\frac{\pi^2 EI}{L}\right)}} \quad (j = 1, 2, \ldots), \tag{40}$$

where j is the sequential number of vibratory modes.

The resulting response amplitudes of the displacement were averaged over the entire longitudinal length for various frequencies of bottom end forced vibrations (Fig. 6). The frequencies associated with the response peaks were regarded as the natural frequencies. Their mode numbers, j, were assigned in increasing order from the smallest peak frequency.

The numerically computed natural frequencies are plotted against the mode sequence number (Fig. 7). The analytical solution (Eq. (40)) is also plotted for comparison. The numerical results are consistent with the analytical results. Thus, adequate performance of the proposed program is verified.

3.2. Design of flexible body

The parameters of the long flexible body were specified by considering the depth and the current speed of the ocean at the site of the structure installation (Table 3). The tension is equivalent to the

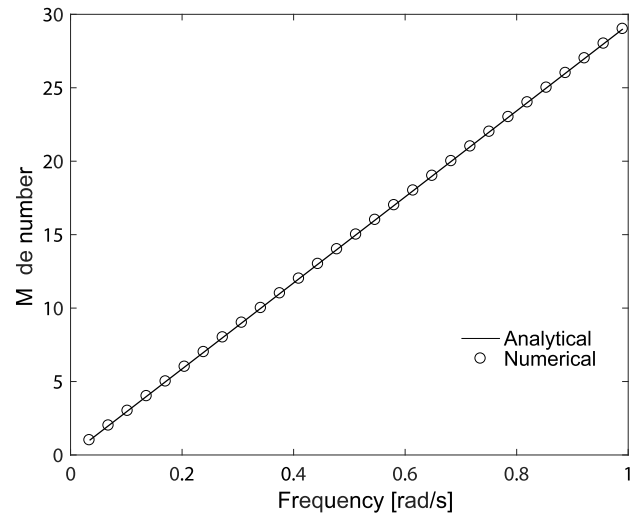

Fig. 7. Relationships between natural frequency and mode number obtained from numerical (circles) and analytical (solid line) calculations.

Table 3
Physical properties of suspended body.

Notation	Definition	Value
L	Whole length	2000 m
d	Outer diameter	0.02 m
d_i	Inner diameter	0.01 m
E	Young's modulus	4.0×10^8 N/m^2
EI	Bending stiffness	2.945 Nm^2
EA	Axial stiffness	9.425×10^4 N
m	Mass per unit length of suspended body	0.5184 kg/m
T	Tension at bottom end	4005.77 N

submerged weight of the flexible body. In this study, the Gulf of Guinea was selected as the installation site because oil and gas reserves were discovered at this location and resource developments have been in operation in this region.

The response amplitudes were calculated (Fig. 8) by performing a frequency domain numerical computation with the parameters inputted. The response amplitudes showed peaks at $\omega = 0.29$, 0.57, and 0.86 rad/s, which are associated with the natural frequencies of the smallest three vibratory modes. Moreover, the natural frequency in Eq. (35) is 0.30 rad/s upon specifying (i) the reduced velocity U^* at which the VIV of a circular cylinder is generally maximized as 6.0, and (ii) the flow speed as 0.006 m/s, which represents the typical flow speed of ocean currents in the deep layer of the installation region. The value of 0.30 rad/s is slightly larger than the smallest value associated with the peaks in Fig. 8.

These results allow us to deduce that the structure vibrates in the form of the first mode or its neighboring modes even when the flow speed is approximately 0.006 m/s, which is notably lower than the typical speeds of the surface current. This aspect will be examined in more detail by performing time-domain simulations.

3.3. Time domain simulation of suspended body

To determine how the suspended body response is related to the vertical distribution of flow speed, time-domain simulations were performed using two vertical distributions of ocean flow speed, that is, those of uniform currents and the Benguela current (the prevailing northward ocean current off the western coast of Africa).

This was followed by a parametric study quantifying how the BEB affects the response. In the standard design (Table 3), the weight of the BEB equals to the weight of the entire suspended body. This parameter

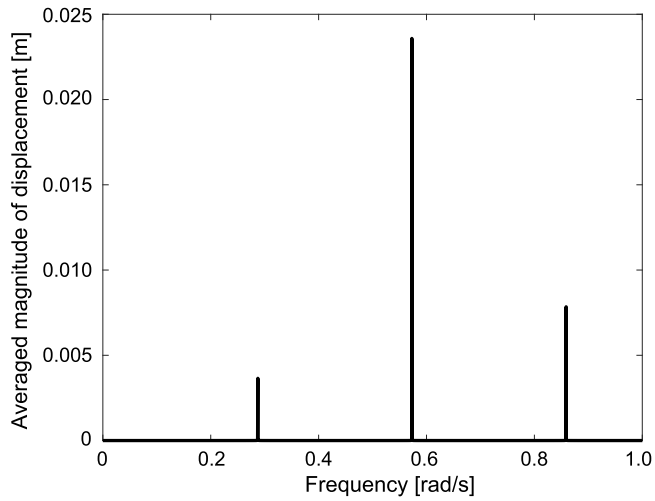

Fig. 8. Magnitude of the displacement averaged over the entire length of suspended body versus frequency.

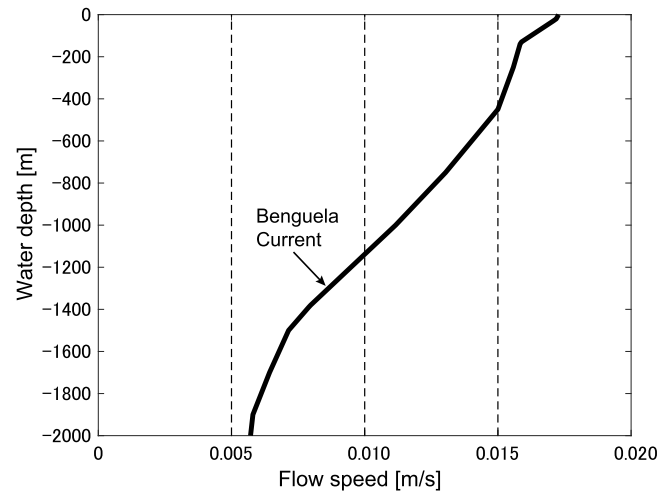

Fig. 9. Vertical profiles of flow speeds of the Benguela current (thicker line) and uniform distribution (vertical straight lines).

Table 4
Simulation cases, ratio of submerged weights (ratio of submerged weight of BEB to that of entire flexible body), and flow speed profile.

Case	Ratio of submerged weights	Flow speed profile
Standard	1.0	Benguela current
B3	3.0	Benguela current
B5	5.0	Benguela current

setting involved uncertainties, thus, three ratios of the BEB weight to that of the entire pipe weight were used (Table 4) to see response sensitivity.

In the following discussion, temporal series and spectra at a specified point (the three-quarter point from the bottom end and middle point: $s/L = 0.75$) are plotted in several figures, because this point clearly exhibits the vibration characteristics and response differences that correspond with changes in BEB mass.

3.3.1. Vertical profile of ocean flow speed

Numerical computations were performed over three uniform distributions (0.0005, 0.0010, and 0.0015 m/s) as well as over the Benguela current distribution using the design parameters listed in Table 3. The vertical distribution of the Benguela current is sheared throughout the water column (Fig. 9). The presented data is based on observations by Richardson and Garzoli (2003). The flow speed is nearly 0.005 m/s at a 2000-m water depth, and gradually increases as the water depth decreases until it reaches 0.017 m/s at the surface.

The uniform distributions provide distinct vibration modal configurations, for which the frequencies are approximately constant. Periodic variations occur at the three-quarter point from the bottom end, (Figs. 10–12). The amplitudes fluctuate for flow speeds of 0.010 m/s, and 0.0150 m/s (Figs. 11 and 12, respectively), whereas for the lowest speed (Fig. 10), the displacement amplitude is almost constant. The amplitude fluctuations arise from the nonuniformity of the tension along the suspended body. The upper part of the body has greater static tension than the lower parts because the former needs to support the weight of the majority of the vertical structure length.

The vibration at the same point for 0.005 m/s has a single predominant frequency of 0.276 rad/s (Fig. 10), which is very close to the natural frequency of the first-mode (Fig. 8), showing that the growth of this vibration results from the synchronization of the vortex shedding frequency to the first mode natural frequency. The dominance of a single component also occurs at 0.010 m/s (Fig. 11) and 0.0150 m/s (Fig. 12). The spectral peaks for the two cases are 0.476 rad/s and 0.675 rad/s, respectively, and their deviations from the natural frequencies (Fig. 8) are large enough to prohibit the synchronization of vortex-shedding frequency with the natural frequencies.

The Benguela current profile yields temporal displacement variations with amplitude fluctuations. The time histories of the three-quarter point from the bottom end are plotted in Fig. 13. The time history of the displacement has maxima (resp. minima) consecutively without down-crossing (resp. up-crossing) the zero point. This irregularity in the temporal variation is evidence of the growth of multiple components with different frequencies. The suspended body used in this study is flexible, thus, the vibration frequency at a point is determined through combining the vortex-shedding frequency at that point with the frequency of the elastic waves that propagate from other points. A similar fluid–structure interaction mechanism was noted by, for example, Vandiver et al. (2009) for an experimental model and Nishi et al. (2018) for an actual-size riser under normal conditions, whereas this study reproduced this result numerically for the suspended body (see also the supplementary animation file).

In contrast to the dynamic transverse displacements, the inline displacements are static after a short initial transient (see also the supplementary animation file). The static state of the inline displacements (Fig. 14) arises primarily from the equilibrium between the hydrodynamic drag ($\mathbf{R}_d$) and gravity ($\mathbf{R}_w$). The Benguela current profile gives a static configuration similar to the uniform profile at 0.01 m/s.

Upon closer observation, the uppermost part recorded for the Benguela current profile is displaced farther downstream when compared to the static displacements recorded for the uniform profile of 0.01 m/s, while the lowermost part is displaced closer to the zero position. This spatial distribution of the static configuration can be explained by observing the Benguela current profile (Fig. 9). The flow speed of the Benguela current is slower than 0.010 m/s in the deep layer, then increases as depth decreases and exceeds 0.015 m/s at the surface layer.

3.3.2. Influence of BEB

For the standard case, the displacement of the middle point ($s/L = 0.5$) irregularly evolves (Fig. 15). The standard case has frequency spectrum with multiple peaks and is very similar to that of the three-quarter point (Fig. 13).

The middle point displacements in cases B3 and B5 have the same irregularities (Figs. 16 and 17, respectively) as the standard case displacement. The frequency spectra of cases B3 and B5 exhibit several peaks (Fig. 16–17), which is similar to the spectrum in the standard

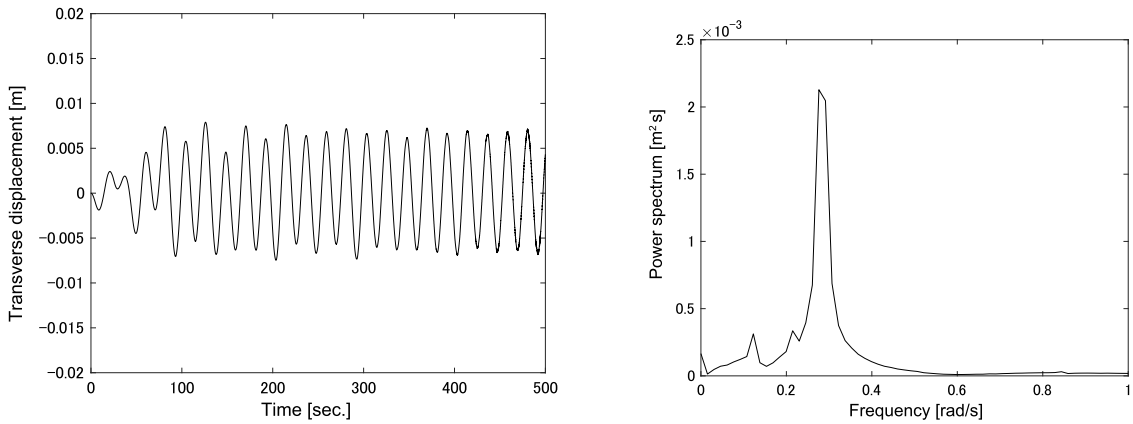

Fig. 10. Results for a uniform flow speed profile of 0.005 m/s. Left: time series of transverse displacement at three-quarter point from bottom end. Right: power spectrum of time series.

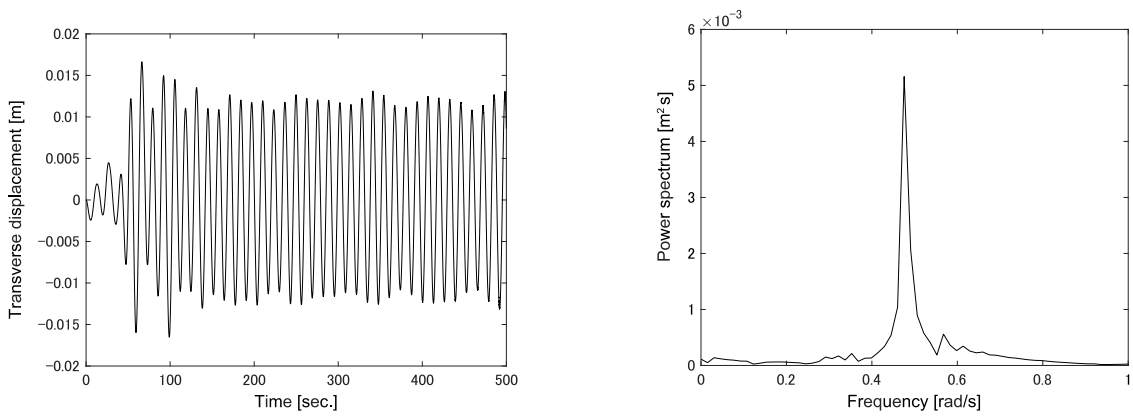

Fig. 11. Results for a uniform flow speed profile of 0.010 m/s. Left: time series of transverse displacement at three-quarter point from bottom end. Right: power spectrum of time series.

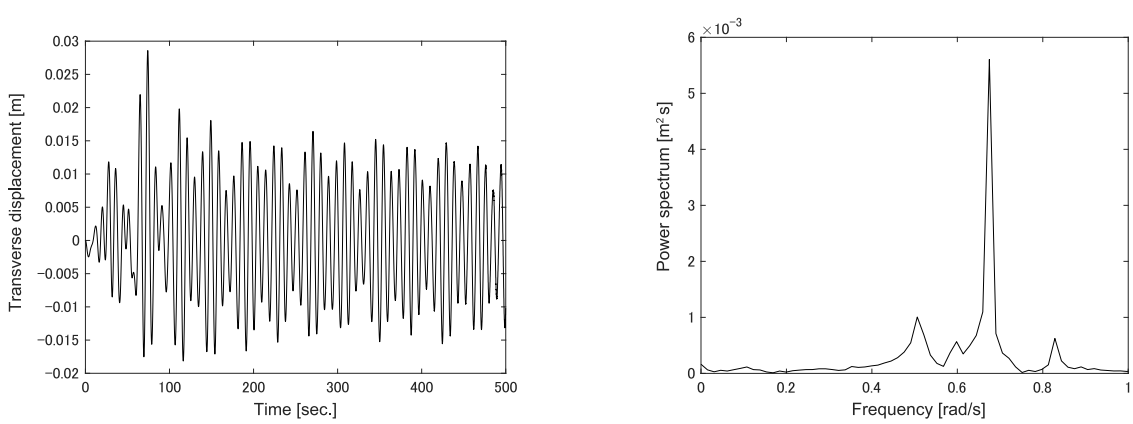

Fig. 12. Results for a uniform flow speed profile of 0.015 m/s. Left: time series of transverse displacement at three-quarter point from bottom end. Right: power spectrum of time series.

case. It is noteworthy that the peak frequencies are higher for cases B3 and B5. The shifts of the spectral peaks are the largest in case B5 (Fig. 17).

The natural frequencies of the suspended body (vertical lines in Fig. 15–17) are related to the BEB weight via the variation in tension. A greater weight leads to higher natural frequencies, which accompany the greater shifts of the spectral peaks. A greater BEB weight corresponds to fewer spectral peaks. It comes from the wider intervals between neighboring natural frequencies in cases B3 and B5.

These results can be interpreted in terms of the fluid–structure interaction mechanics. The faster flow speeds in shallow layer (Fig. 9) excite vibrations with higher frequencies, and the slower flow speeds in the deeper layer excite lower frequency vibrations. The multiple spectral peaks (Figs. 13, and 15–17) are caused by the downward propagation of elastic waves excited in the upper part in addition to the upward propagation of waves excited in the lower part. The excitation intensity depends on the differences between the multiple vortex-shedding frequencies and the natural frequencies. If the vortex-shedding frequencies and the natural frequencies are very close, the former is entrained

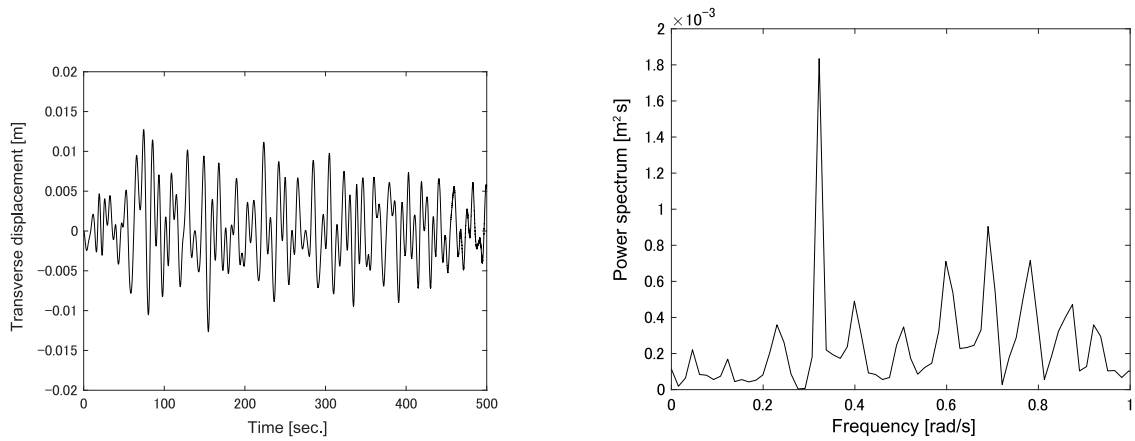

Fig. 13. Results for the Benguela current profile. Left: time series of transverse displacement at three-quarter point from bottom end. Right: power spectrum of time series.

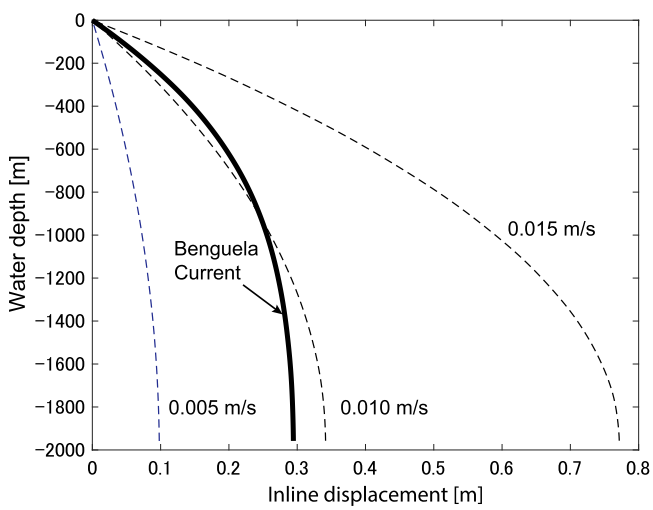

Fig. 14. Inline displacements of suspended body.

into the latter, and the VIVs of the corresponding modes grow. A lighter (resp. heavier) BEB causes the suspended body to have relatively lower (resp. higher) natural frequencies with narrower (resp. wider) intervals between the neighboring natural frequencies. It follows that more (resp. fewer) modes are excited by a lighter (resp. heavier) BEB through the synchronizations of the vortex-shedding frequency and the corresponding natural frequencies.

The amplitudes of the transverse vibrations exhibit modal configurations (Fig. 18). The amplitudes at the bottom end are smaller than those at the upper parts because the BEB motion is suppressed by the drag and inertial forces acting on it. A heavier BEB yielded smaller amplitudes overall with the maximum of the root-mean-square (RMS) amplitude equating to 25% of the outer diameter of the pipe.

Although the developed model performed well under the assumptions made in this study, the following aspects were not considered and must be resolved in future work. (1) The inline VIV component was omitted in this model because it is generally smaller than the transverse component. (2) The method constructed herein can be refined by validating its performance against the results obtained from experiment and computational fluid dynamics. (3) The vertical-profile data of the Benguela current speeds was temporally constant and excluded time-varying aspects such as tidal currents. (4) The Benguela current was assumed to flow in a single direction (x-direction), but in fact it flows in different directions at different depths.

4. Conclusions

A numerical model was developed to simulate the fluid–structure interaction mechanics of a long flexible underwater body that is suspended from the free surface. The model comprised structural, vortex-induced force and BEB models. These characteristics were coupled to represent their mechanical interactions. The governing equations of the structural model were solved using the Kellor box method, the vortex-induced force was computed by applying the wake-oscillator model, and the BEB equation was solved considering tensions of the suspended body acting on the BEB. By using vertical profiles of ocean current speeds, numerical simulations were performed, and the results were analyzed. The following conclusions are drawn from these analyses.

- The proposed numerical model adequately combines the three sets of dynamics (structural, vortex-induced force, and BEB), and simulates the fluid–structure interaction of the suspended body.
- The actual vertical profile of the Benguela current speed promotes the growth of multiple frequency components (Figs. 13, and 15–17).

The numerical model facilitates the simulation of the dynamic motion and static deformation of a suspended body and allows for a more refined design.

Declaration of competing interest

The authors declare that they have no known competing financial interests or personal relationships that could have appeared to influence the work reported in this paper.

Acknowledgment

This study was supported financially by the Japan Society for the Promotion of Science (JSPS) Grand-in-Aid for Scientific Research 18H01636.

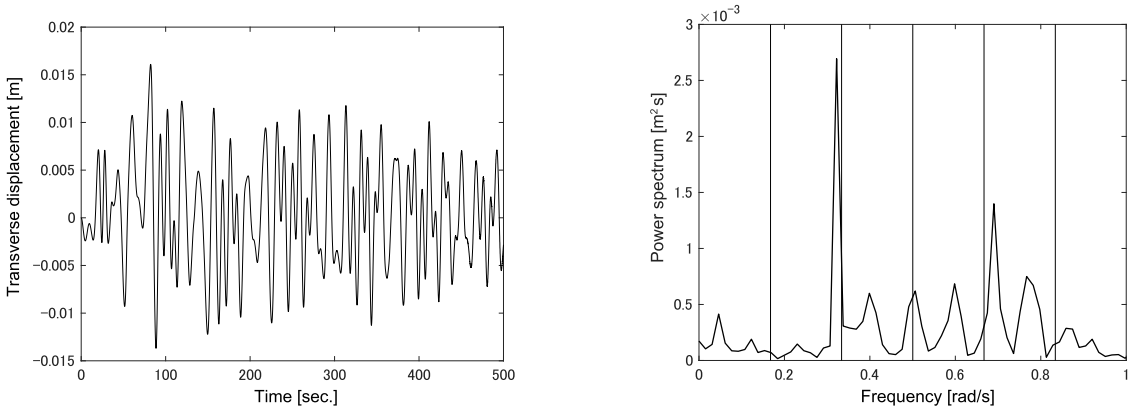

Fig. 15. Results for the standard case. Left: time series of transverse displacement at middle point. Right: power spectrum of time series. Vertical lines indicate natural frequencies of suspended body.

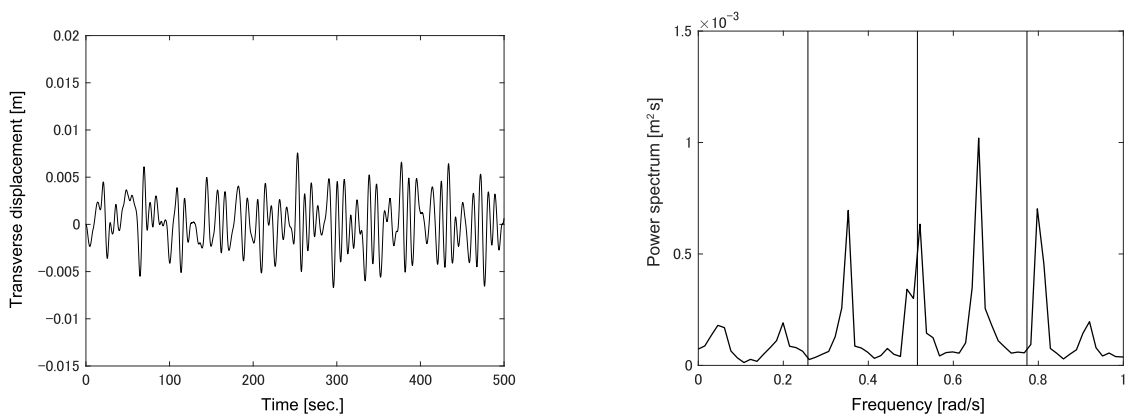

Fig. 16. Results for case B3. Left: time series of transverse middle point displacement. Right: power spectrum of time series. Vertical lines indicate natural frequencies of suspended body.

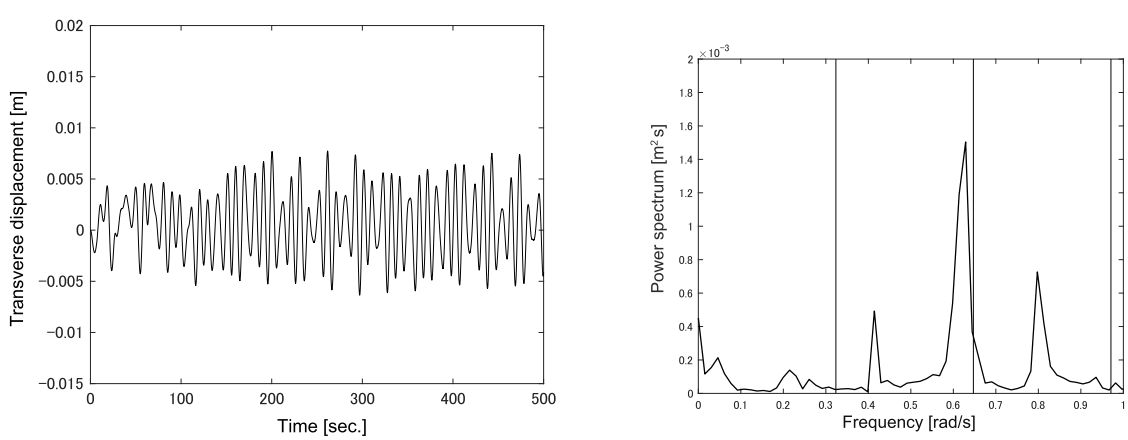

Fig. 17. Results for case B5. Left: time series of transverse middle point displacement. Right: power spectrum of time series. Vertical lines indicate natural frequencies of suspended body.

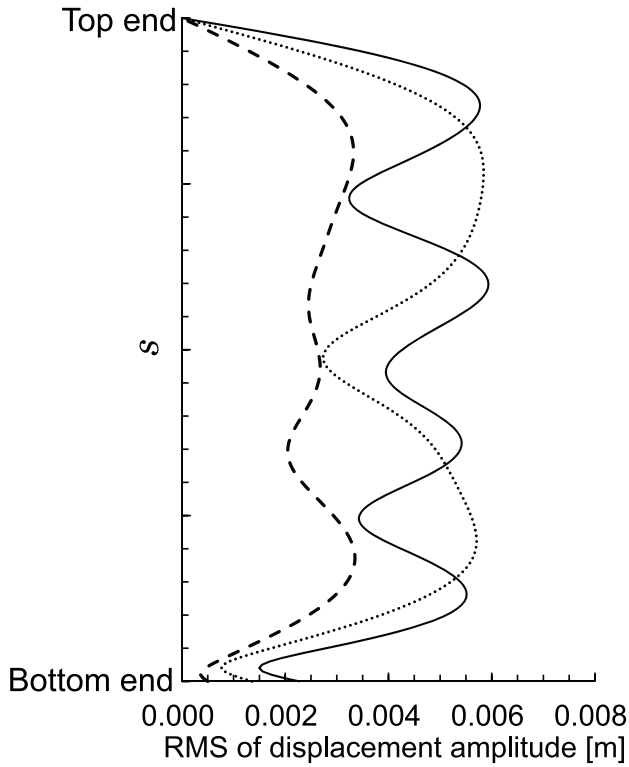

Fig. 18. Vertical distributions of the transverse vibration root-mean-square (RMS) amplitudes: standard case (solid line), case B3 (dotted line), and case B5 (dashed line).

Appendix A

The coefficient matrix **M** is expressed as

$$\mathbf{M} = \begin{bmatrix} 0 & 0 & 0 & -m & 0 & 0 & 0 & 0 & -mw & mv\cos\theta \\ 0 & 0 & 0 & 0 & -m+m_{\mathrm{a}} & 0 & 0 & 0 & 0 & -m\left(u\cos\theta + w\sin\theta\right) \\ 0 & 0 & 0 & 0 & 0 & -m+m_{\mathrm{a}} & 0 & 0 & mu & mv\sin\theta \\ -\frac{1}{EA} & 0 & 0 & 0 & 0 & 0 & 0 & 0 & 0 & 0 \\ 0 & 0 & 0 & 0 & 0 & 0 & 0 & 0 & 0 & -\left(1+\frac{T}{EA}\right)\cos\theta \\ 0 & 0 & 0 & 0 & 0 & 0 & 0 & 0 & 1+\frac{T}{EA} & 0 \\ 0 & 0 & 0 & 0 & 0 & 0 & 0 & 0 & 0 & 0 \\ 0 & 0 & 0 & 0 & 0 & 0 & 0 & 0 & 0 & 0 \\ 0 & 0 & 0 & 0 & 0 & 0 & 0 & 0 & 0 & 0 \\ 0 & 0 & 0 & 0 & 0 & 0 & 0 & 0 & 0 & 0 \end{bmatrix}. \tag{41}$$

The coefficient matrix **K** is expressed as

$$\mathbf{K} = \begin{bmatrix} 1 & 0 & 0 & 0 & 0 & 0 & 0 & 0 & 0 & 0 \\ 0 & 1 & 0 & 0 & 0 & 0 & 0 & 0 & 0 & 0 \\ 0 & 0 & 1 & 0 & 0 & 0 & 0 & 0 & 0 & 0 \\ 0 & 0 & 0 & 1 & 0 & 0 & 0 & 0 & 0 & 0 \\ 0 & 0 & 0 & 0 & 1 & 0 & 0 & 0 & 0 & 0 \\ 0 & 0 & 0 & 0 & 0 & 1 & 0 & 0 & 0 & 0 \\ 0 & 0 & 0 & 0 & 0 & 0 & EI & 0 & 0 & 0 \\ 0 & 0 & 0 & 0 & 0 & 0 & 0 & EI & 0 & 0 \\ 0 & 0 & 0 & 0 & 0 & 0 & 0 & 0 & 1 & 0 \\ 0 & 0 & 0 & 0 & 0 & 0 & 0 & 0 & 0 & \cos\theta \end{bmatrix}. \tag{42}$$

The vector **F** is expressed as

$$\mathbf{F} = \begin{bmatrix} S_{\mathrm{b}}\Omega_2 - S_{\mathrm{n}}\Omega_3 - \omega_0\sin\phi\cos\theta + R_{\mathrm{dt}} \\ \Omega_3\left(T + S_{\mathrm{b}}\tan\theta\right) - \omega_0\cos\phi + R_{\mathrm{dn}} \\ -S_{\mathrm{n}}\Omega_3\tan\theta - T\Omega_2 - \omega_0\sin\phi\sin\theta + R_{\mathrm{db}} \\ \Omega_2 w - \Omega_3 v \\ \Omega_3\left(u + w\tan\theta\right) \\ -\Omega_3 v\tan\theta - \Omega_2 u \\ EI\Omega_3^2\tan\theta - S_{\mathrm{b}}\left(1+\frac{T}{EA}\right)^3 \\ -EI\Omega_2\Omega_3\tan\theta + S_{\mathrm{b}}\left(1+\frac{T}{EA}\right)^3 \\ -\Omega_2 \\ -\Omega_3 \end{bmatrix}. \tag{43}$$

Appendix B. Supplementary data

Supplementary material related to this article can be found online at https://doi.org/10.1016/j.oceaneng.2019.106723.

References

Bai, Y., Bai, Q., 2005. Subsea Pipelines and Risers, first ed. Elsevier.

Blevins, R.D., 1977. Flow-Induced Vibrations, first ed. van Nostrand Reinhold Company.

Chatjigeorgiou, I.K., 2008. A finite differences formulation for the linear and nonlinear dynamics of 2d catenary rises. Ocean Eng. 35, 616–636.

Chatjigeorgiou, I.K., 2010. On the effect of internal flow on vibrating catenary risers in three dimensions. J. Eng. Struct. 32, 3313–3329.

Chen, W.I., Zhang, Q.Q., Li, H., Hu, H., 2015. An experimental investigation on vortex induced vibration of a flexible inclined cable under a shear flow. J. Fluids Struct. 54, 297–311.

Doan, V.P., Nishi, Y., 2015. Modeling of fluid–structure interaction for simulating vortex-induced vibration of flexible riser: finite difference method combined with wake oscillator model. J. Mar. Sci. Technol. 20, 309–321.

Hoffman, J.D., 1992. Numerical Methods for Engineers and Scientists, first ed. McGraw-Hill.

Honghai, F., Chaowei, L., Zhiming, W., Liangbin, X., Yu, W., Xu, F., 2016. Dynamic analysis of a hang-off drilling riser considering internal solitary wave and vessel motion. J. Natural Gas Sci. Eng. 37, 512–522.

Howell, C.T., 1992. Investigation of the Dynamics of Low Tension Cables (Ph.D. thesis). Massachusetts Institute of Technology.

Kajiwara, H., Noridomi, K., 2009. Reentry control system design for riser pipe experimental model under steady current. In: Proceedings of ICCAS-SICE International Joint Conference. Fukuoka, Japan.

Koterayama, W., Nakamura, M., Kajiwara, H., Matsui, H., Noridomi, K., 2008. Development of a training simulator for dynamic reentry operations of a riser pipe hanged off. In: Proceedings of the Eighteenth International Offshore and Polar Engineering Conference. Vancouver, Canada, pp. ISOPE–I–08–410.

Nishi, Y., Doan, V.P., 2015. Distribution of damping device on riser pipe in sheared currents. Ocean Eng. 104, 489–499.

Nishi, Y., Kokubun, K., Hoshino, K., Uto, S., 2009. Quasisteady theory for the hydrodynamic forces on a circular cylinder undergoing vortex-induced vibration. J. Mar. Sci. Technol. 14 (3), 285–295.

Nishi, Y., Motoyoshi, M., Ueda, T., 2018. Growth and coexistence of structural and lift force modes in vortex-induced vibration of a flexible riser. J. Mar. Sci. Technol. 23 (4), 899–914.

Ohtsubo, K., Senga, H., Manabe, T., Koterayama, W., Kajiwara, H., 2005. Experimental study on reentry operation of a flexible marine riser by gain-scheduled control. J. Japan Soc. Naval Archit. Ocean Eng. 2, 49–55.

Patel, M.H., Jesudansen, A.S., 1987. Theory and model tests for the dynamic response of free hanging risers. J. Sound Vib. 112 (1), 146–166.

Richardson, P.L., Garzoli, S.L., 2003. Characteristics of intermediate water flow in the benguela current as measured with rafos floats. Deep-sea Res. II 50, 87–118.

Sarpkaya, T., Isaacson, M., 1981. Mechanics of Wave Forces on Offshore Structures, first ed. Van Nostrand Reinhold Company.

Shengwei, W., Xuesong, X., Xiang, L., 2016. Movement optimization of freely-hanging deepwater risers in reentry. Ocean Eng. 116, 32–41.

Srinil, N., 2011. Analysis and prediction of vortex-induced vibrations of variable-tension vertical risers in linearly sheared currents. Appl. Ocean Res. 33, 41–53.

Sumer, B.M., Fredsœ, J., 1997. Mechanics of Wave Forces on Offshore Structures, first ed. World Scientific Publishing.

Suzuki, H., Yoshida, K., Ishida, S., Nam, D., 1994. Active control of riser deformation and vessel motion for automatic entry/reentry system. In: Proceedings of the Fourth International Offshore and Polar Engineering Conference. Osaka, Japan, pp. ISOPE–I–94–120.

Suzuki, H., Yoshida, K., Nam, D., Murai, M., Usami, A., Ishida, S., 1993. Basic research on the automatic reentry of deepwater riser by active control. J. Soc. Naval Archit. Japan 174, 865–874.

Triantafyllou, M.S., Triantafyllou, G.S., 1991. The paradox of the hanging string: an explanation using sigular perturbations. J. Sound Vib. 148 (2), 343–351.
Trim, A.D., Braaten, H., Lie, H., Tognarelli, M.A., 2005. Experimental investigation of vortex-induced vibration of long marine risers. J. Fluids Struct. 21 (3), 335–361.
Tsukada, R.I., Morooka, C.K., 2016. A numerical procedure to calculate the VIV response of a catenary riser. Ocean Eng. 122, 145–161.
Vandiver, J.K., Allen, D., Li, L., 1996. The occurrence of lock-in under highly sheared conditions. J. Fluids Struct. 10, 555–561.
Vandiver, J.K., Jaiswal, V., Jhingran, V., 2009. Insights on vortex-induced, traveling waves on long risers. J. Fluids Struct. 25, 641–653.
Violette, R., de Langre, E., Szydlowski, J., 2007. Computation of vortex-induced vibrations of long structures using a wake oscillator model: Comparison with dns and experiments. Comput. Struct. 85, 1134–1141.
Wang, S., Xu, X., Yao, B., Lian, L., 2012. A finite difference approximation for dynamic calculation of vertical free hanging slender risers in re-entry application. China Ocean Eng. 26 (4), 637–652.
Wenbo, W., Jiasong, W., Zhongxu, T., Shixiao, F., Zhengli, L., Junfeng, L., Rongyao, W., Leijian, S., Juanjuan, Q., 2014. Dynamic analysis on drilling riser evacuated in hard hang-off mode. In: Proceedings of the Twenty-fourth International Ocean and Polar Engineering Conference. Busan, Korea, pp. ISOPE–I–14–189.
Wilson, J.F., 2002. Dynamics of Offshore Structures, second ed. John Wiley & Sons.
Yanbin, W., Deli, G., Jun, F., 2014a. Static analysis of deepwater marine riser subjected to both axial and lateral forces in its installation. J. Natural Gas Sci. Eng. 19, 84–90.
Yanbin, W., Deli, G., Jun, F., 2014b. Study on lateral vibration analysis of marine riser in installation-via variational approach. J. Natural Gas Sci. Eng. 22, 523–529.